SAND2024-03390J

The Effect of Grain Boundary Facet Junctions on Segregation and Embrittlement

M.E. Fernandez[1], R. Dingreville[2], D.L. Medlin[3], D.E. Spearot[1,*]

[1] Department of Mechanical & Aerospace Engineering, University of Florida, Gainesville, FL, 32611, USA
[2] Center for Integrated Nanotechnologies, Sandia National Laboratories, Albuquerque, NM, 87185, USA
[3]Sandia National Laboratories, Livermore, CA, 94551, USA
* Corresponding author: dspearot@ufl.edu, 352-392-6747

Abstract

Junctions are discontinuities in flat grain boundaries that arise in all polycrystalline materials and are thought to play important roles in the response of a grain boundary network to thermal and mechanical loads. A key open question concerns the mechanisms by which solute segregation to junctions impacts properties of the grain boundary. In this work, we investigate the influence of grain boundary facet junctions on solute embrittlement, and we present an analytical model that uses the hydrostatic stress field contributed by dislocations at multiple junctions to describe these effects. Specifically, we study junctions between {112} facets of various lengths in Au ⟨111⟩ Σ3 tilt grain boundaries. Copper and silver solutes are employed to determine if the effect of junctions on solute segregation and embrittlement is dependent on size relative to the host. Combined, atomistic simulation data and the analytical model show that Cu and Ag have opposite segregation responses to junctions due to the sign of the hydrostatic stress field induced by junctions. However, a positive shift in the embrittling potency is computed near junctions regardless of solute type

or the stress state of the segregation site. Hence, for the conditions studied, junctions consistently shift the energetic landscape towards embrittlement.

Keywords

Grain boundaries, Facet junctions, Solute segregation, Solute embrittlement

1. Introduction

A grain boundary (GB) is an internal interface between misoriented crystals (grains) within a polycrystalline material. The atomic structure of grain boundaries can be complex and depends on parameters such as composition, crystal geometry, and temperature. Grain size is generally used to predict bulk material characteristics, including yield strength and fracture resilience [1–3], the emission of dislocations in metals [4,5], and the stability of nanocrystalline metals [6–8]. GBs in polycrystalline metal alloys serve as sites for solute segregation, creating concentration gradients which can impact alloy properties [9–15], such as GB mobility and grain growth stabilization in metals [16,17].

If a long, flat GB is energetically unfavorable due to its inclination, the flat GB may transition into a non-planar boundary composed of connected lower energy facets [18], introducing higher surface area and facet junctions in exchange for more energetically favorable structural units at the interface. Junctions may naturally contain dislocation or disclination content to accommodate the change in inclination between facets [18].

Several studies have captured a GB undergoing faceting or defaceting transitions during changes in temperature using atomistic simulations or phase field modeling [19–23]. Structural analysis by Medlin et al. identified patterns of dislocation content in faceted Σ5 STGBs which accommodate slight misorientation from the ideal Σ5 angle [18]. Other studies have captured how facets move in response to stress [24] or how solute segregation can reduce facet migration velocity [25]. In this study, we are interested in the capacity of the facet junction to influence solute segregation and embrittlement. We expect that facet junctions containing defect content will create segregation and anti-segregation zones, following work from Hu et al. [26,27] on GB disconnections. Additionally, work on triple

junctions from Tuchinda and Schuh suggests that junctions generally experience higher concentrations of solutes compared to the adjacent GBs, which becomes especially important as grain size decreases [28].

Solute segregation to a GB affects solute embrittlement, whereby the energy of formation of two free surfaces (FSs) from a grain boundary is altered due to the presence of solutes [29]. Thermodynamically, the embrittlement effect is measured using embrittling potency, which is the difference in energy between segregation to the grain boundary and to the FS. Most atomistic calculations of embrittlement, using either density functional theory or interatomic potentials, have focused on flat GBs; however, some recent works have evaluated solute embrittlement in broader contexts, such as in large data sets for theoretical polycrystalline embrittlement [30] or with large variation in FS geometry [31]. However, the study of embrittlement has not previously been extended to facet junctions between two or more boundaries. Here, we consider the specific case of facet junctions, but we expect the concepts from this study to be extendable to more general boundary intersections, such as triple junctions. Additionally, analytical models of embrittlement extrapolated from atomistic data could be upscaled for use in higher length scale modelling techniques, such as phase field fracture [32–34].

Thus, the objective of this work is to quantify the extent to which junctions act as embrittling agents by comparing embrittling potencies between flat and faceted GBs. Specifically, we model a series of grain boundary geometries in the Au $\Sigma 3 \langle 111 \rangle$ system composed of {112} facets, including a flat GB for comparison. Using molecular statics (energy minimization) calculations, we compute solute segregation energies and embrittling

potencies near the junction for Cu and Ag solutes. These simulations motivate an analytical model that employs the hydrostatic stress provided by dislocation content from multiple junctions to capture the effect of junctions on solute segregation and embrittling potency.

2. Model Construction

2.1. Material Selection, Interatomic Potential, and Software

The structure of Σ3 {112} facets and their geometry in faceted Σ3 ⟨111⟩ GBs is well-documented in Au and other FCC metals [35–39], providing opportunity for validation of the atomistic model. Hence, we choose Au as the bulk (solvent) material, with Cu and Ag solutes. This material system provides two solvent-solute pairs, Au-Cu and Au-Ag, where in the former the solute is smaller than the solvent, and the opposite is true in the latter. This material system allows us to test whether or not the size difference results in contrasting segregation and embrittlement behavior due to opposite hydrostatic stresses from the substitutional defect [40–42].

We use the LAMMPS atomistic simulation software [43] to perform molecular statics calculations using a nonlinear conjugate gradient method for energy minimization, and we use OVITO [44] for visualizing the model structures and segregation data. For the interatomic potential, we choose an embedded-atom method (EAM) potential designed by Zhou et al. [45]. This potential is fit to stacking-fault energies and enthalpies of mixing closely, making it suitable for GB geometry and solute segregation. The precise numerical results we present in Sections 3 and 4 are sensitive to material choice and interatomic potential, but work from Hu et al. showed that across several different material combinations, dislocations affect segregation in consistent ways, irrespective of material

choice [26,46]. Hence, the fundamental conclusions pertaining to solute segregation and embrittlement around junctions should remain consistent regardless of the choice of solute or potential, since, as will be shown, the embrittlement is primarily dependent on the proximity and orientation of the junctions.

2.2. Grain Boundary Models

The GB model with periodic facets and junctions is shown in Fig. 1(a). The horizontal Σ3 ⟨111⟩ {112} STGB planes, called "horizontal facets" in this work, have $2l$ length. The horizontal facets are separated by a height h and joined by "sloped facets" of projected length s with identical GB geometry but inclined by 120°. The length l and height h are parameterized by the repeating distance of the unit crystal in the $[1\bar{1}0]$ and $[\overline{11}2]$ directions respectively; hence, we refer to the precise lengths and heights by integer multiples of these repeating distances, L and H. Thus, the model geometry is a periodic structure composed of flat peaks and troughs with a trapezoid wave form. Note, the designation of horizontal facet and sloped facet here is chosen based on our reference frame and is ultimately arbitrary.

Compared to a flat GB at the mean inclination, the faceted model geometry is of higher free energy. However, the purpose of this model design is not to study faceting or defaceting energetics, as has been explored previously [18–21]. Instead, this model geometry is designed for analyzing solute segregation and embrittlement, for which many it has many advantages. The length of the horizontal and sloped facets can be constructed using integer multiples of the repeating lattice distances in the ⟨110⟩ and ⟨112⟩ directions, respectively. Hence, it is straightforward to construct a set of models with different facet lengths and heights, but with the same crystallographic junction geometry, which will be used to

compare the effects of junction separation distances on segregation energies. Additionally, the simple repeating structure is compatible with periodic boundary conditions in ⟨110⟩, ⟨112⟩ and [111] directions, eliminating edge effects. A detailed description of how this model is constructed is available in the supplemental material.

We perform segregation energy calculations for 20 GBs over a range of L and H, including $L \in (2, 4, 6, 8)$ and $H \in (0, 2, 4, 6, 8)$. The region for segregation analysis is set to a 20 Å radius circle around the junction positioned at $(x,z) = (-l, -h)$. This circular region is sufficiently large to observe the transition between GB and bulk behavior for sites around the junction. Additionally, we add rectangular segregation regions 30 Å wide along the adjacent sloped and horizontal facets, to observe the evolution from junction site to facet site behavior. These regions are illustrated in Fig. 1(a).

As an example, the minimum energy structure of the $L = 8, H = 8$ facetted GB is shown in Fig. 1(b). The structure at the GB is a 9R crystal structure, shown in Fig. 1(c). This is common for metals with low stacking fault energies like Au [35,36]. For all $H > 0$, facet

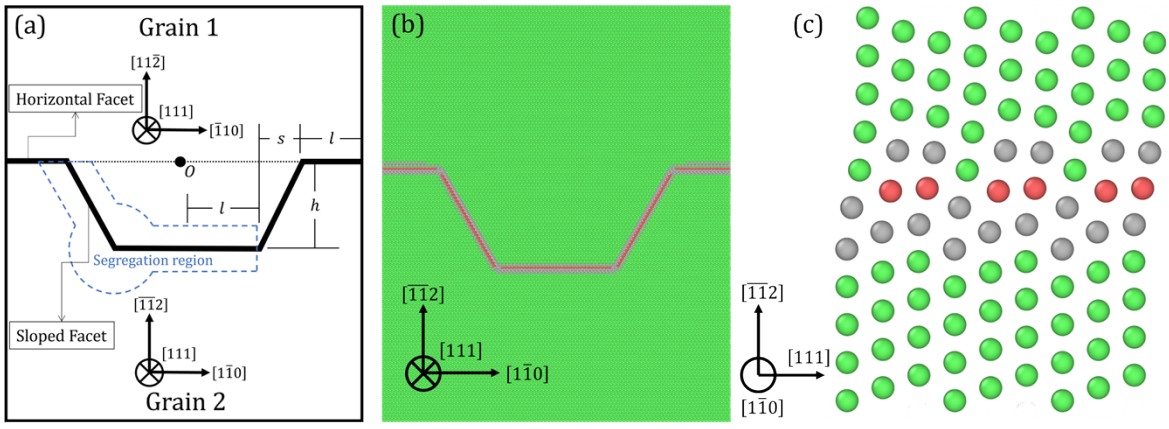

Figure 1: (b) The $L = 8, H = 8$ GB model. Atoms are colored by common neighbor analysis, where red atoms are identified as HCP, green atoms as FCC, and white atoms as neither. (c) Cross-section of the GB showing the 9R stacking structure.

junctions are located at $(x,z) = (l + s,0), (l, -h), (-l, -h), (-l - s,0)$. Each junction connects a sloped facet and horizontal facet, so we expect the junctions to contain dislocations within the same family. However, a typical Burgers circuit provides a misleading answer in this case, an example of which is shown in supplemental Fig. S1.

Instead, we compute the intrinsic dislocation content from the rigid body translation incompatibility between adjacent facets. Ideally, each grain should terminate at coincident sites at the GB to minimize intrinsic interfacial strain; however, limitations from the crystal geometry may prevent the formation of such an idealized surface. We can compute a rigid body translation between the ideal geometry and the real geometry by finding the distance between would-be coincidence atoms [47–49]. When GB facets terminate at a junction, the rigid body translations of each facet combine and, if they do not annihilate, produce a geometric incompatibility that manifests at the junction as an intrinsic dislocation. In Fig. 2, we measure the rigid body translations of grains on individual $\{111\}$ planes near the $(l + s,0)$ junction. For consistency, the line direction of the translations is counterclockwise about the junction, and we use the coordinate frame of the lower grain for measurement. Note, we choose this orientation so that hydrostatic stress predictions from the measured Burgers vectors match the sign conventions of the simulations, as discussed in Section 4.1.

We find two locations where the rigid body displacement is observable: on the horizontal facet in the A plane the translation is $\frac{2.7219}{\sqrt{6}}[\bar{1}\bar{1}2] + \frac{0.0210}{\sqrt{2}}[1\bar{1}0]$ Å, and on the sloped facet in the B plane the translation is $-\frac{1.2581}{\sqrt{6}}[\bar{1}\bar{1}2] + \frac{2.419}{\sqrt{2}}[1\bar{1}0]$ Å. Note that there is no rigid body translation on the C plane. The sum of these rigid body translations is approximately $1.1382[1\bar{2}1]$ Å or $0.2790a[1\bar{2}1]$. Thus, each junction accommodates the

transition between sloped and horizontal facets with a $0.2790\langle 112\rangle$ type edge dislocation. Junctions on the same sloped facet but different horizontal facet have oppositely signed Burgers vectors, i.e., the complement to $\boldsymbol{b} = 0.2790[1\bar{2}1]$ in the $(l+s,0)$ junction is $\boldsymbol{b} = 0.2790[\bar{1}2\bar{1}]$ in the $(l,-h)$ junction. Additionally, the $(-l-s,0)$ junction has $\boldsymbol{b} = 0.2790[2\bar{1}\bar{1}]$ vector, and the $(-l,-h)$ junction has $\boldsymbol{b} = 0.2790[\bar{2}11]$. Ultimately, since each junction has dislocation content, each junction contributes a local stress field [50] that influences the segregation behavior of solutes, as will be discussed in Section 4.1.

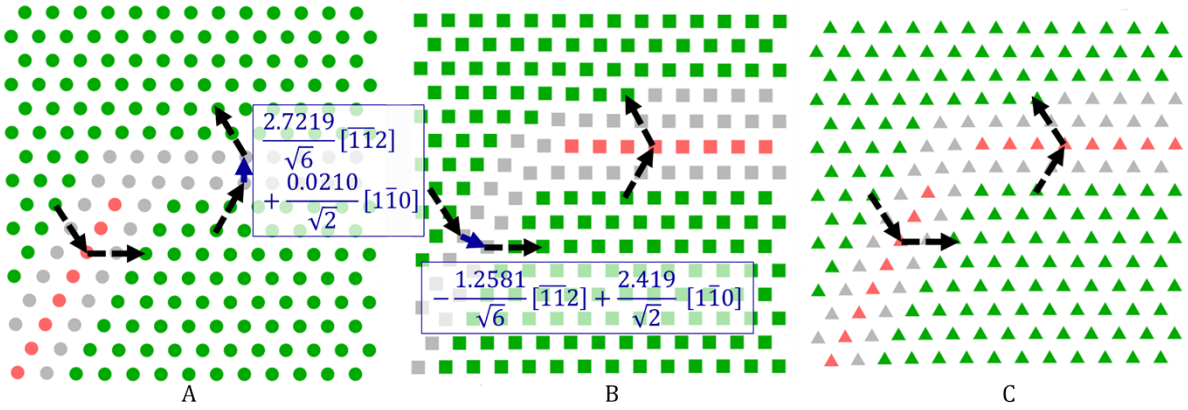

Figure 2: Diagram of the rigid body displacement in each of the three unique atomic layers, labeled A, B, and C. Similar crystallographic directions are indicated with black arrows, suggesting would-be coincidence sites, while the rigid body translation vectors are shown schematically by blue arrows with formula in the corresponding equation boxes.

2.3. Free Surface Models

To compute embrittling potencies, we create appropriate FS models. There are many potential cleavage paths we could choose to create FSs in our junction model, both transgranular and intergranular. We choose an intergranular cleavage path for two reasons: intergranular fracture is energetically favorable for embrittled GBs [51] and aligning the

cleavage path with the GB assures that the proximity of the FS to a particular site type remains constant. So, from a set of multiple intergranular cleavage paths, we choose a minimum energy FS for embrittlement analysis. A more detailed discussion on how we model these FSs is available in the supplemental material.

We compute both relaxed (minimized) and unrelaxed (pre-minimization) excess free energies for a set of 15 FSs. Considering both energies is necessary to ensure that the choice of minimum energy FS is physically plausible, though generally the pre-minimization energy is more important, as discussed in works by Mai et al. [52–54]. As shown in Fig. 3(a), the clear minimum energy surface in both relaxed and unrelaxed states is the "-1" surface, shown in Fig. 3(b), so we choose this surface for embrittlement study.

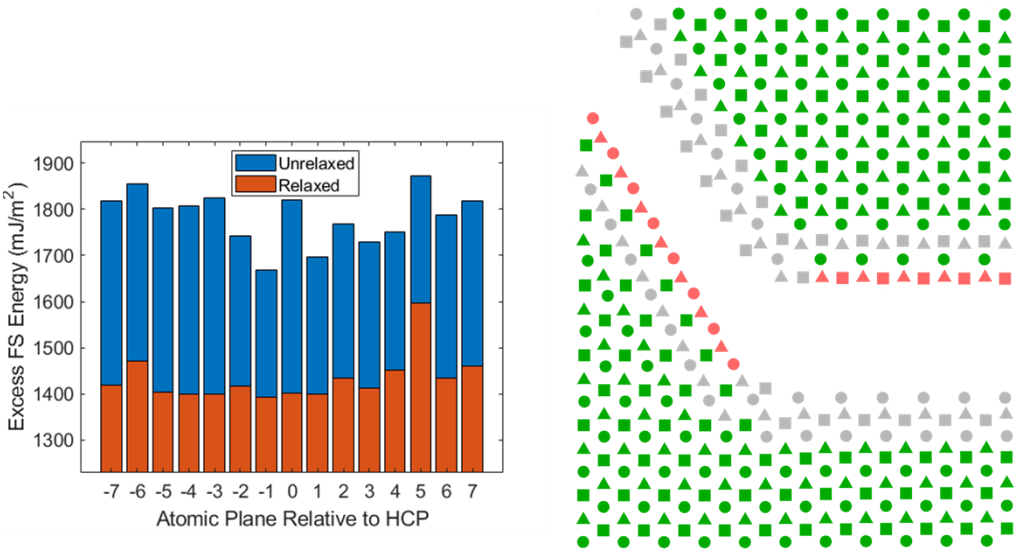

(a) (b)

Figure 3: (a) Bar plots comparing the FS excess energy before and after minimization, where the x axis denotes the atomic plane above or below the original HCP plane. (b) FS -1, the minimum energy surface chosen from analysis of (a).

2.4. Segregation Energy and Embrittling Potency

The segregation energy for any site i, whether at a GB or a FS, can be calculated as a difference of two quantities: the energy of swapping the solute into a GB or FS site (denoted GB/FS), and of swapping the solute into a bulk site [55–57],

$$\Delta E_{seg,i}^{GB/FS} = E_i^{GB/FS} - E^{bulk}. \quad (1)$$

To compute $\Delta E_{seg,i}^{GB/FS}$, we insert a solute at a bulk site with lowest centrosymmetry [58] and potential energy closest to the bulk energy of Au prescribed by the interatomic potential, which is the site least disturbed by effects from the GB facets or junctions. We then minimize and compute the total potential energy as E^{bulk}. Likewise, for each GB/FS site i, we individually swap in a solute to that site and compute the total potential energy $E_i^{GB/FS}$. Note, we use the relaxed total energy for computing $\Delta E_{seg,i}^{GB}$, but for $\Delta E_{seg,i}^{FS}$, we use the unrelaxed total energy, since in a fracture context, the embrittling potency is only important in the immediate moment after fracture, when the FS is unrelaxed [52–54]. This also eliminates uncertainty resulting from reconstruction of the FS after minimization. We note that $\Delta E_{seg,i}^{GB/FS} < 0$ implies segregation, while $\Delta E_{seg,i}^{GB/FS} > 0$ implies anti-segregation.

Embrittling potency can be calculated as the difference in segregation energy for the GB and FS configurations [29],

$$\Delta E_{b,i} = \Delta E_{seg,i}^{GB} - \Delta E_{seg,i}^{FS}. \quad (2)$$

In this formulation, $\Delta E_{b,i} > 0$ denotes embrittling, while $\Delta E_{b,i} < 0$ denotes strengthening. We note that each segregation site i has a unique embrittling potency that is highly dependent on the geometry of the FS [31].

3. Results

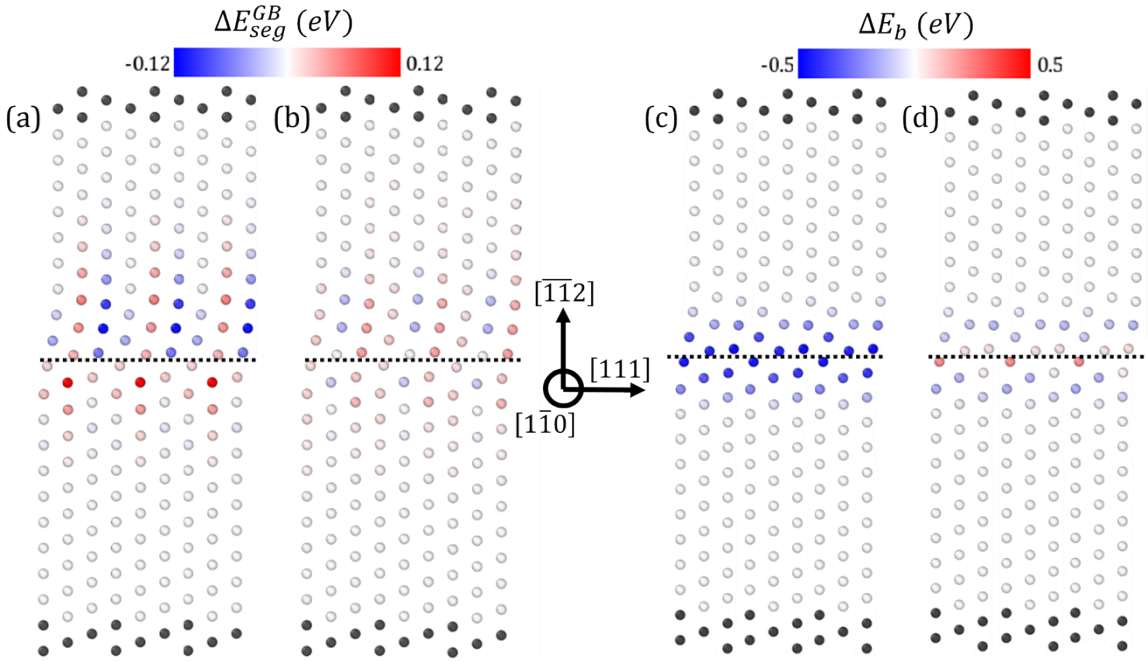

Figure 4: Segregation energy profiles around the flat GB for (a) Cu solutes and (b) Ag solutes. Embrittling potency profiles around the flat GB with (c) Cu solutes and (d) Ag solutes. Segregation profile viewed from the side of the 9R structure. The dashed line indicates the position of the fracture plane.

Figure 4 shows the segregation energy and embrittling potency for sites around the flat GB for both Cu and Ag solutes, viewed along a cross-section looking down the ⟨110⟩ x-axis. Since the repeating distance of the GB structure in the ⟨110⟩ direction is short, this side view fully displays the solute segregation character of the GB. We observe bending of {111} planes through the 9R structure, corresponding to where the segregation energies and embrittling potencies are of greatest magnitude.

The magnitude of the segregation energies for Cu solutes is generally larger than those for Ag solutes. As seen in Figs. 4(a) and (b), many of the sites which are segregation (blue) for Cu become anti-segregation sites (red) for Ag, and vice versa. This behavior is likely related to their atomic volume when compared to Au. As shown by Liu and Adams [11],

Cu is drawn to compressed atomic sites to mitigate tensile elastic strain energy from being embedded in the lattice of larger Au atoms, while Ag is drawn to atomic sites in tension to mitigate compressive elastic strain energy since Au is slightly smaller. In Figs. 4(c) and (d), the magnitudes of embrittling potency are greatest near the position of the cleavage plane indicated by the dashed line, and the size effect is less obvious. Ag shows some embrittling behavior, whereas Cu is a strengthener for nearly all atomic sites. For both segregation and embrittlement, the energies for Cu solutes are generally higher in magnitude compared to Ag solutes.

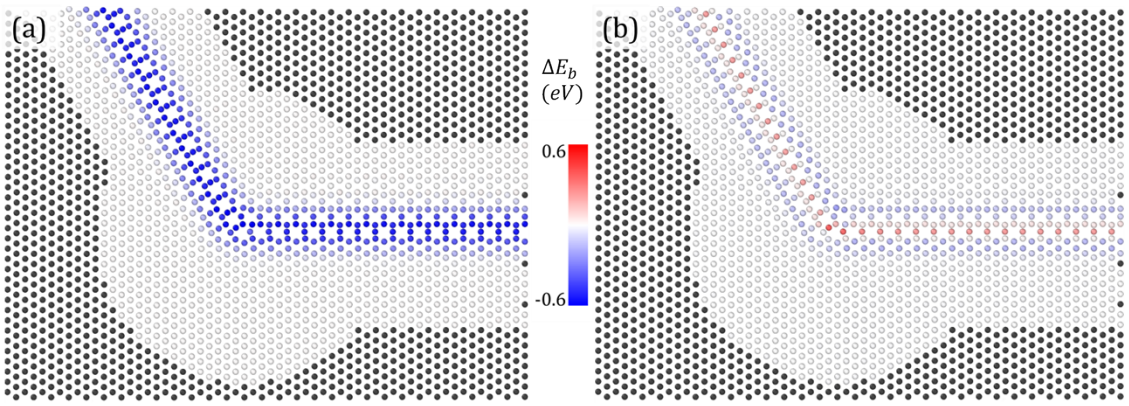

Figure 5: Embrittling potency profile around an $L = 8, H = 8$ GB junction for (a) Cu solutes and (b) Ag solutes.

Embrittlement around the GB junctions is more complex. Figure 5 shows embrittling potencies around the $(-l, -h)$ junction in the $L = 8, H = 8$ GB. To quantify the effect of the junction, we define a segregation energy difference between the faceted and flat GB, $\Delta E_{seg,i}^{GB} - \Delta E_{seg,i}^{GB,flat}$ and an embrittling potency difference, $\Delta E_{b,i} - \Delta E_{b,i}^{flat}$. $\Delta E_{seg,i}^{GB,flat}$ and $\Delta E_{b,i}^{flat}$ denote the GB segregation energy and embrittling potency, respectively, to a particular site type i in the flat GB, while $\Delta E_{seg,i}^{GB}$ and $\Delta E_{b,i}$ denote GB segregation energy and embrittling

potency, respectively, to a particular site type i in models containing junctions. This difference isolates the contribution of the junctions to segregation and embrittlement on a site-by-site basis. Note, $\Delta E_{seg,i}^{GB} - \Delta E_{seg,i}^{GB,flat} > 0$ implies reduced preference for segregation at site i with respect to the flat GB. Similarly, $\Delta E_{b,i} - \Delta E_{b,i}^{flat} > 0$ implies a shift towards embrittlement for site i with respect to the flat GB.

We choose the atomic site type located one atomic plane above the HCP plane, shown graphically in Fig. 6(a), because it lies in the layer of uniformly pro-segregation sites closest to the FS for Cu solutes. While Ag has anti-segregation behavior for this site, this is expected from the converse size effects of both solutes, and it is still necessary to choose this site for comparative similitude. We then plot the effect of the junctions on segregation, $\Delta E_{seg,i}^{GB} - \Delta E_{seg,i}^{GB,flat}$, and embrittlement, $\Delta E_{b,i} - \Delta E_{b,i}^{flat}$, to that site against distance from the junction. This is shown for all H and L with Cu solutes in Fig. 6(b) and 6(c) respectively. Data for the Ag solutes are provided in Fig. 7. Note, $L = 2$ GBs contain segregation data spanning the full length of the horizontal facet to show the mirror symmetry. Other GBs only show data that spans half the length of the horizontal facet.

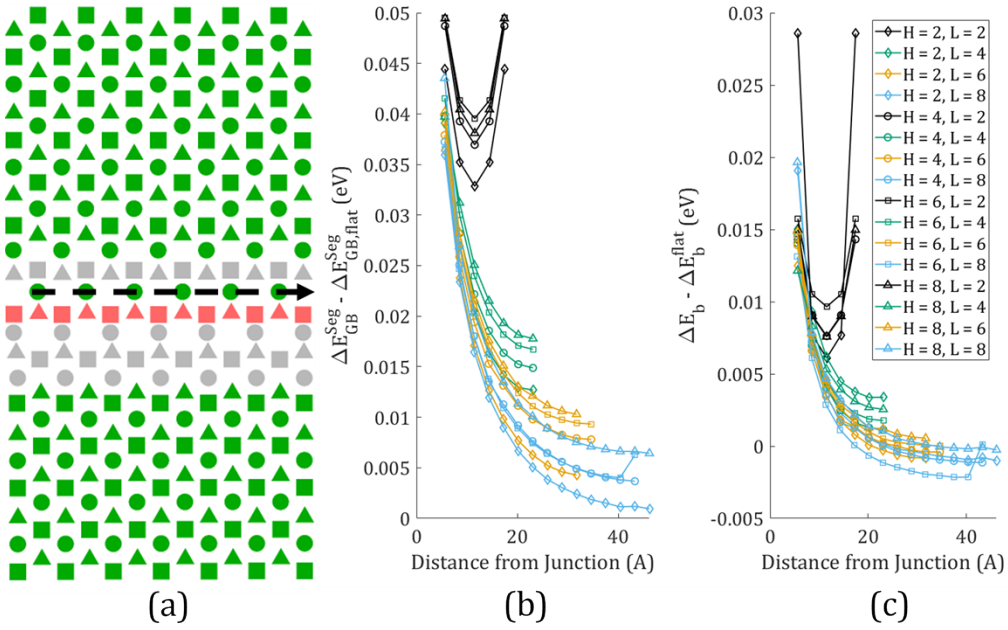

Figure 6: (a) The site type plotted is shown with a dashed arrow, alongside plots of the (b) segregation energy difference and (c) embrittling potency difference as a function of distance from the junction for Cu solutes.

Figure 6(b) and 7(b) shows that as the distance from the junction increases, the segregation energy difference $\Delta E_{seg}^{GB} - \Delta E_{seg}^{GB,flat}$ decreases until the midpoint between junctions is reached. We find that the lowest magnitude value of $\Delta E_{seg}^{GB} - \Delta E_{seg}^{GB,flat}$ is given by the$L = 8$,$H = 2$ GB for both Cu and Ag, which suggests that the proximity between the junctions along the sloped facet causes a screening of their stress fields, diminishing the effect of junctions on segregation energy at a distance along the horizontal facet. This screening effect and more aspects of junction-solute and junction-junction interactions will be discussed in Section 4.2.

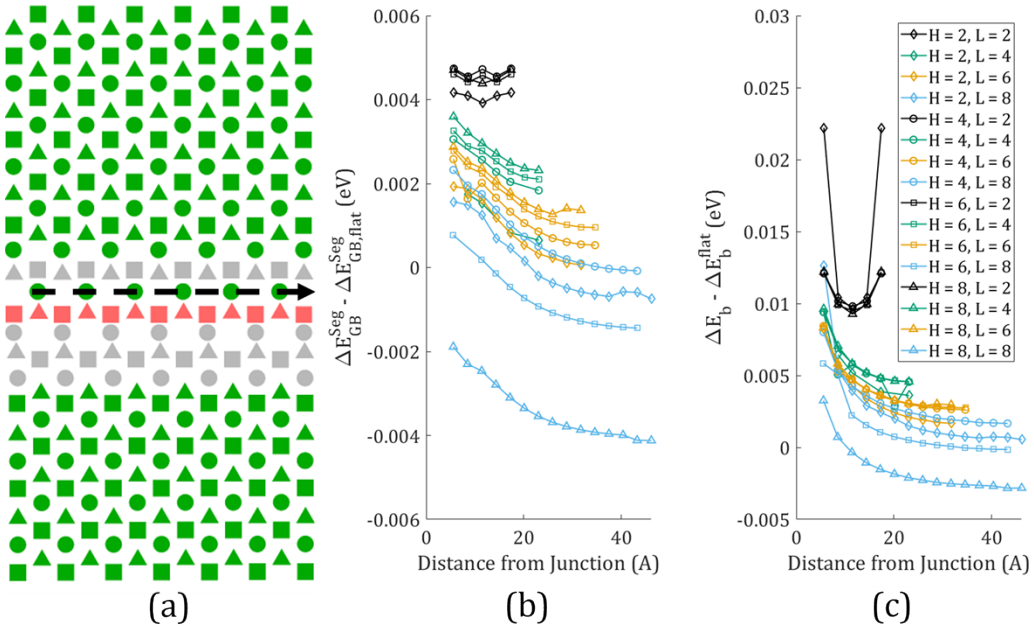

Figure 7: (a) The site type plotted is shown with a dashed arrow, alongside plots of the (b) segregation energy difference and (c) embrittling potency difference as a function of distance from the junction for Ag solutes.

The embrittling potency difference $\Delta E_{b,i} - \Delta E_{b,i}^{flat}$ retains many features from the segregation energy difference, as shown in Fig. 6(c) and 7(c). Specifically, the functional forms remain broadly the same, and the $L = 8, H = 2$ GB shows the smallest magnitude change relative to the flat GB. Note that the positive shift in embrittling potency for Cu solutes near junctions does not lead to embrittlement itself. As Fig. 5(a) demonstrates, none of the sites for Cu solutes have positive embrittling potency (i.e., they are all strengthening sites). In this case, a $\Delta E_{b,i} - \Delta E_{b,i}^{flat} > 0$ with small magnitudes shown in Fig. 6(c) implies a decrease in the strengthening effect of Cu solutes. For the case of Ag solutes, where embrittling sites exist and the embrittling potency difference is positive near junctions, proximity to the junction provides an increase in the embrittling effect of Ag solutes, as shown in Fig. 7(c).

Thus, in both cases, the embrittling potency experiences a positive shift near junctions, which indicates that atomic size mismatch is not a dominating factor in the effect of junctions on solute induced embrittlement. Instead, the intrinsic geometry of the junction itself is responsible for the solute embrittlement. We develop an analytical relationship between junction geometry and the embrittling potency in Section 4.2.

Note, for the chosen potential, the heats of mixing for Cu in Au and Ag in Au are respectively $q_{mix}^{Cu-Au} = -0.3898\ eV$ and $q_{mix}^{Ag-Au} = -0.0787\ eV$. Comparing these quantities to the results in Figs. 6 and 7, we see that Cu generally has greater magnitude segregation energy differences, as suggested by its greater magnitude heat of mixing. Interestingly, for both solutes, the embrittling potency differences are of similar magnitude, suggesting that the increase in embrittling potency has more to do with the junctions than the solutes

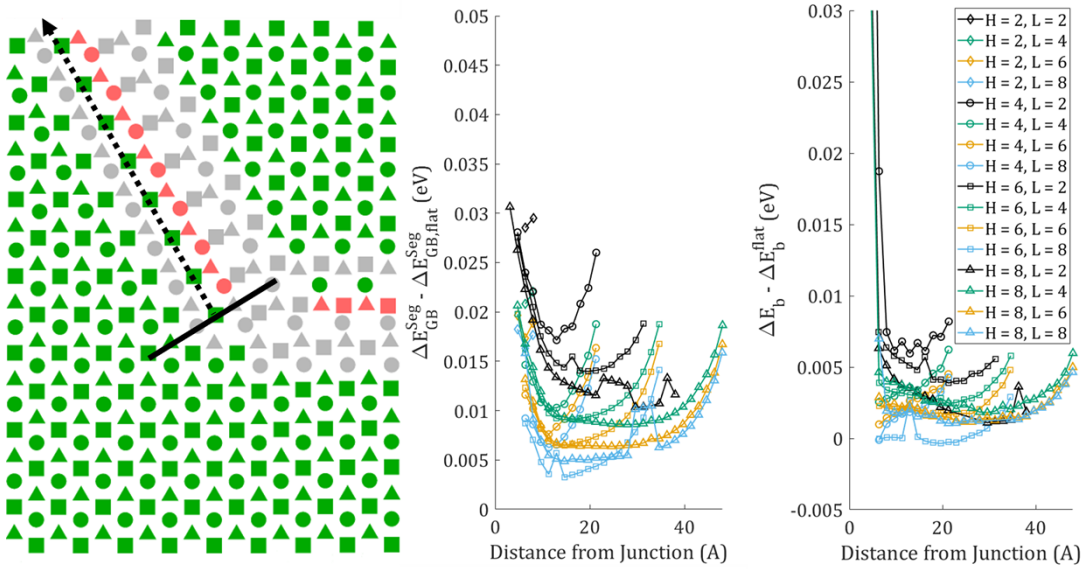

(a) (b) (c)

Figure 8: (a) Plane of atoms targeted for calculations along the sloped facet. Note the plane is the same site type as in Fig. 6, but it is in the opposite crystal. (b) Segregation energy difference and (c) embrittling potency difference versus distance from the junction for Cu solutes.

themselves. We discuss this phenomenon more in Section 4.3.

We perform similar analysis for the same atomic site type along the sloped facet. Figure 8 shows the transition from the $(-l,-h)$ junction (located at 0 on the abscissa) to the $(-l-s,0)$ junction (rightward on the abscissa) for Cu solutes. Data for the Ag solutes are provided in Fig. 9. Note that the plane of sampled atomic sites is in crystal 2 on the opposite side of the facet since the structure flips orientation upon crossing the junction. Additionally, while the noise in Fig. 9 may appear large, this noise is on the order of 10^{-3} eV, which is well within the computational convergence error for these large simulations.

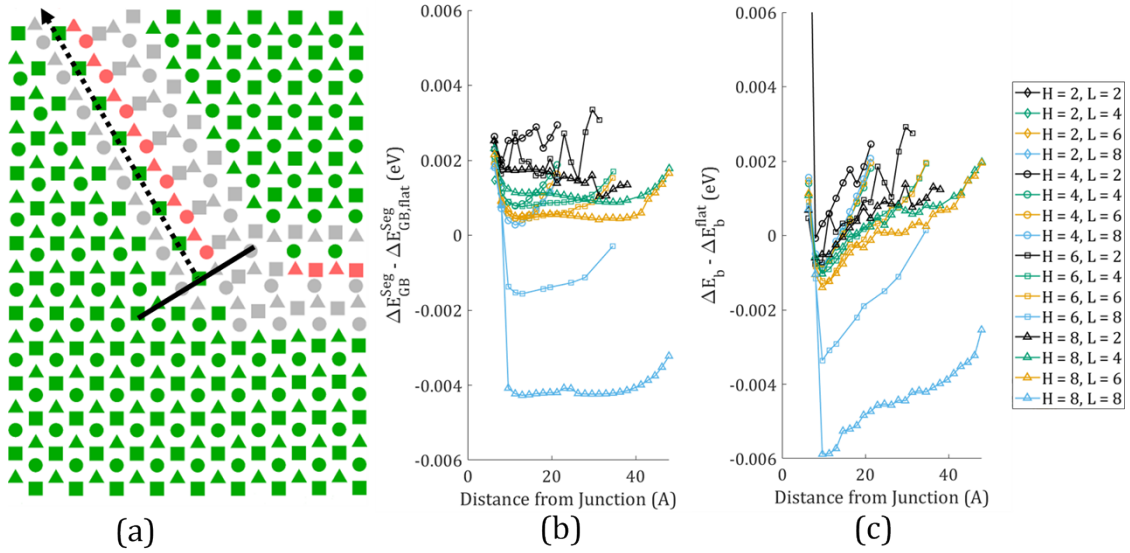

Figure 9: (a) Plane of atoms targeted for calculations along the sloped facet. (b) Segregation energy difference and (c) embrittling potency difference versus distance from the junction for Ag solutes.

In Fig. 8(b) and 9(b), the near-junction points for segregation energy difference (left side of the plot) do not start at the same energy as the near-junction points in Fig. 6(b) or 7(b). This is because, even though site type is identical, the positions of the starting sites are on opposite sides of the junction. Note, the segregation energy difference in Fig. 8(b) and

9(b) and embrittling potency difference in Fig. 8(c) and 9(c) have mostly positive peaks at both ends of the plot, even though the positions of these sites are on opposite sides of the nearest junction. Importantly, positive peaks in the embrittling potency difference plot imply that proximity to the junction increases embrittling potency. Hence, junctions act as embrittling agents in a thermodynamic sense for the chosen FS and the chosen atomic site.

Note that in the cases of Figs. 6 – 9, the values of these segregation energy and embrittling potency differences are on the order of 10^{-2} or $10^{-3}\ eV$, about an order of magnitude smaller than segregation energies and embrittling potencies on the flat GB for Cu or Ag. It is imperative to account for this difference despite its apparent magnitude because solutes will be attracted more to the junctions than to the facets. The impact of junctions in polycrystals on segregation patterns at a GB has been shown to be important [28], even if the as-measured segregation energy differences are relatively small. Additionally, these results highlight that the presence of solutes at the junction weakens the GB against fracture more than solutes segregated to a pristine GB. Especially in nanocrystalline metals where material properties are controlled by properties of the GBs and solute segregation is paramount in stabilizing grain size [59], this impact of segregated solutes on fracture resilience near the junction cannot be ignored.

4. Discussion

4.1. Junction Stress Fields

Figure S2 in the supplemental materials shows that segregation energy at each atomic site in all models follows a generally linear relationship with the hydrostatic virial stress at that site [11]. Hence, the stress fields resulting from each junction should have a predictable

effect on segregation energy. At the center of each junction is an edge dislocation which generates a stress field. For an edge dislocation, Hirth and Lothe [50] derived the hydrostatic stress field analytically as,

$$\sigma_{hydro}(b;x,z) = -\frac{\mu b}{2\pi(1-\nu)}\frac{z}{r^2} \ . \tag{3}$$

Here, μ is the elastic modulus, b is the magnitude of the Burgers vector, ν is Poisson's ratio, and $r = \sqrt{x^2 + z^2}$ is the position relative to the dislocation core, using the coordinate system for the facetted models in this work.

The Cartesian representation of Eq. (3) is defined such that the Burgers vector aligns with the x-axis. Alternatively, if $z = r\sin\theta$, where $\sin\theta = \frac{|\boldsymbol{b}\times\boldsymbol{r}|}{|\boldsymbol{r}||\boldsymbol{b}|}$, and $\boldsymbol{r}$ is the vector position relative to the dislocation core, a vector representation of Eq. (3) is,

$$\sigma_{hydro}(\boldsymbol{b},\boldsymbol{r}) = \mp\frac{\mu}{2\pi(1-\nu)}\frac{|\boldsymbol{b}\times\boldsymbol{r}|}{|\boldsymbol{r}|^2} \ , \tag{4}$$

where the sign of the equation is either negative or positive depending on if the angle from $\boldsymbol{b}$ to $\boldsymbol{r}$ about the dislocation core axis is positive or negative, respectively. Then, the total stress field resulting from all j dislocations (*i.e.*, junctions) in the system can be written as $\sum_j \sigma_{hydro}(\boldsymbol{b}_j,\boldsymbol{r}_j)$. Note, Eqs. (3) and (4) are true for an isotropic, infinite medium. Our models are not infinite mediums in all directions, though the model contains periodic boundary conditions and is designed with a large distance between the model boundaries and the facets such that their interaction can be ignored. Au has a reported Zener ratio of 2.92 [60], which is not isotropic at the crystal level.

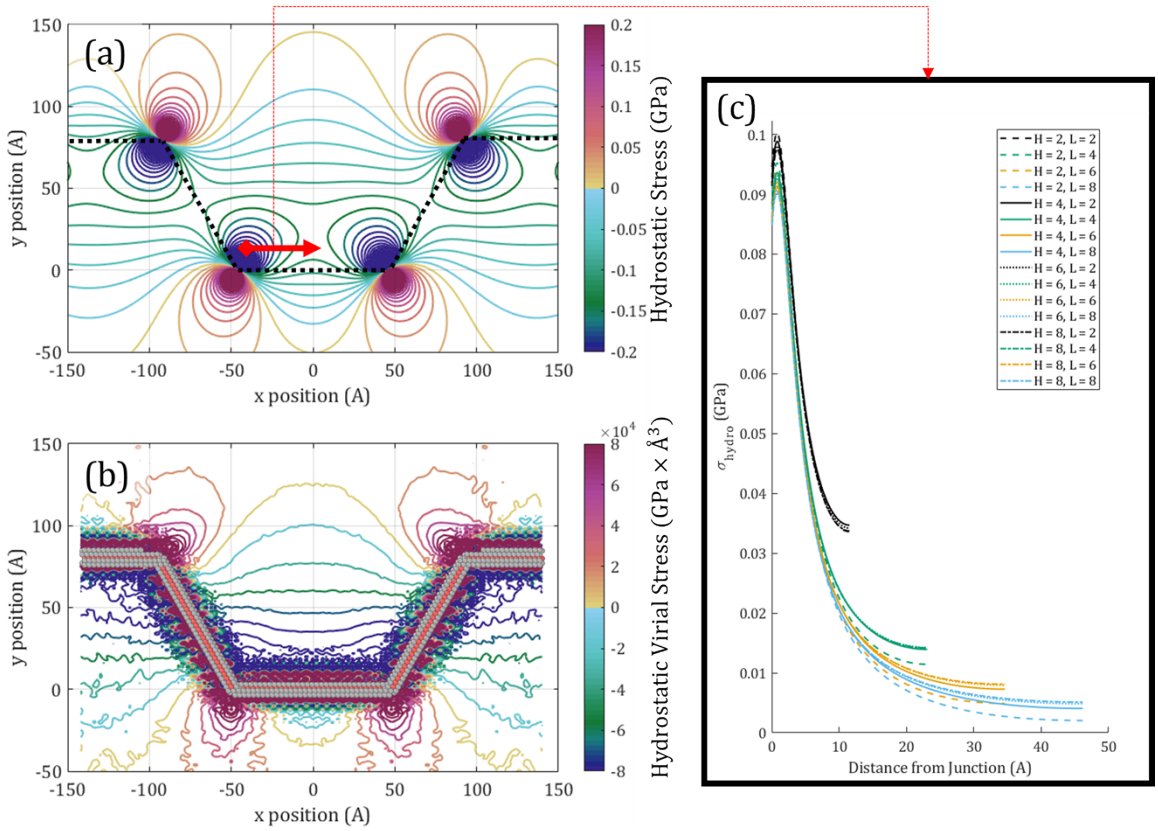

Figure 10: (a) Contour plot of the analytical hydrostatic stress field of junction dislocations in the $H = 8, L = 8$ GB. The GB is indicated by dotted lines. Note, the GB is contained within the compressive region of stress. (b) Contours of hydrostatic virial stress computed from atomistic model for comparison. The atoms at the grain boundary, identified by CNA, are overlayed for geometric clarity (c) Analytical hydrostatic stress along the contour specified by the arrow.

To assess how important the deviation from isotropy is, we compare the analytical hydrostatic stress and simulated hydrostatic virial stress for the $L = 8$, $H = 8$ GB in Fig. 10(a) and (b). The contour plots in Fig. 10(b) are generated by binning atomic virial stresses based on the atom coordinates, averaging, and then taking the contour over that binned average. The analytical contour plot in Fig. 10(a) matches well with the hydrostatic virial stresses computed from the atomistic model, as shown in Fig. 10(b). Hence, Eq. (3) serves as a good approximation of the hydrostatic stress for edge dislocations in our model.

Note, Fig. 10(b) highlights both the long-range stress fields of junction dislocations and the short-range stress fields of the GB itself. Since Fig. 10(a) only plots the analytical functions of hydrostatic stress for the dislocations at the junctions, this short-range stress field is not captured. The short-range stress field around the GB shows an alternating pattern of high tensile and compressive regions, reminiscent of those predicted by disclination models of GBs [61–63].

Motivated by the relationship between segregation energy and hydrostatic stress, we analytically compute a slice of the σ_{hydro} field using the same coordinate orientations as Fig. 8; this plot is shown in Fig. 10(c). This analysis reveals that as distance from the junction increases along this contour, σ_{hydro} decreases to a minimum between the two junctions. As the height H decreases, σ_{hydro} decreases due to junction-junction screening. We recover analytically that the $H = 2, L = 8$ GB produces the lowest σ_{hydro}, which correlates with the trends in segregation energy differences observed in Fig. 8. Hence, hydrostatic stress is a good indicator of the segregation behavior, in accordance with classical stress-dependent isotherms for segregation [11]. Interestingly, the sloped region from Fig. 8(a) and 9(a) transitions between regions of hydrostatic compression and hydrostatic tension, as shown in Fig. 10, while the embrittling potency difference remains positive near both junctions in Fig. 8(c) and 9(c). This contrast suggests that only proximity to the junction is important for embrittlement, and not necessarily the sign of the stress state.

4.2. Relationship Between Junctions and Segregation

Since embrittlement is fundamentally a difference between segregation energies, we first develop an analytical expression for the energy of segregation to a site around a junction

$\Delta E_{seg,i}^{GB}$. Such an expression should include the segregation energy to a site in a flat GB, $\Delta E_{seg,i}^{GB,flat}$, the contribution from the junctions, E_{jxn}, and junction-junction interactions $E_{jxn-jxn}$. Note, these are not the excess energies of the facet junctions or their interaction pairs, normalized by the length of the dislocation line at the junction, but rather the specific impact of those features on the segregation (and embrittlement in the following section) of a solute to a particular atomic site. Hence, these terms will have units of eV. We employ a superposition of these terms to compute the segregation energy,

$$\Delta E_{seg,i}^{GB} = \Delta E_{seg,i}^{GB,flat} + E_{jxn} + E_{jxn-jxn}. \quad (5)$$

In the limit that no junctions are present, $\Delta E_{seg,i}^{GB} = \Delta E_{seg,i}^{GB,flat}$ clearly returns the flat GB segregation energy. From analysis in Section 4.1, we expect E_{jxn} to have a form that is similar to the formula for hydrostatic stress caused by dislocation content. Additionally, since the presence of the junction core cannot be described completely by theory of elasticity, E_{jxn} should include a core effect term E_{core}. In total, E_{jxn} is described by,

$$E_{jxn}(r) = c \sum_{j} \frac{|\boldsymbol{b}_j \times \boldsymbol{r}_j|}{|\boldsymbol{r}_j|^2} + E_{core}\,, \quad (6)$$

where the sum is over every junction dislocation j. c is a fitting constant with units of eV, and we do not treat this as a constant with respect to site or model geometry. Hence, we fit c to minimize the residual standard error (RSE) of E_{jxn} compared to the segregation energy difference $\Delta E_{seg,i}^{GB} - \Delta E_{seg,i}^{GB,flat}$ computed using the $H = 8, L = 8$ model for a chosen site type. We specifically choose the $H = 8, L = 8$ model because we expect the least junction-junction interactions in this model. Note, unlike in Eq. (4), the sign of the magnitude of $|\boldsymbol{b}_j \times \boldsymbol{r}_j|$ is irrelevant here. As per observation in Fig. 9, compression or tension from the junction

presence do not seem to matter, only proximity to the junction. This prediction matches nicely with results from Tuchinda and Schuh [28], where a similar trend is observed for segregation in Al based alloys.

For E_{core} and $E_{jxn-jxn}$ terms, we lump these together into a constant e with units of eV. The e term is fit to minimize the RSE error for every model, while c remains constant as the fit value from the $H = 8, L = 8$ model. Fitting this way reveals how the effects of the junctions that cannot be easily described via elasticity theory change with varying H and L.

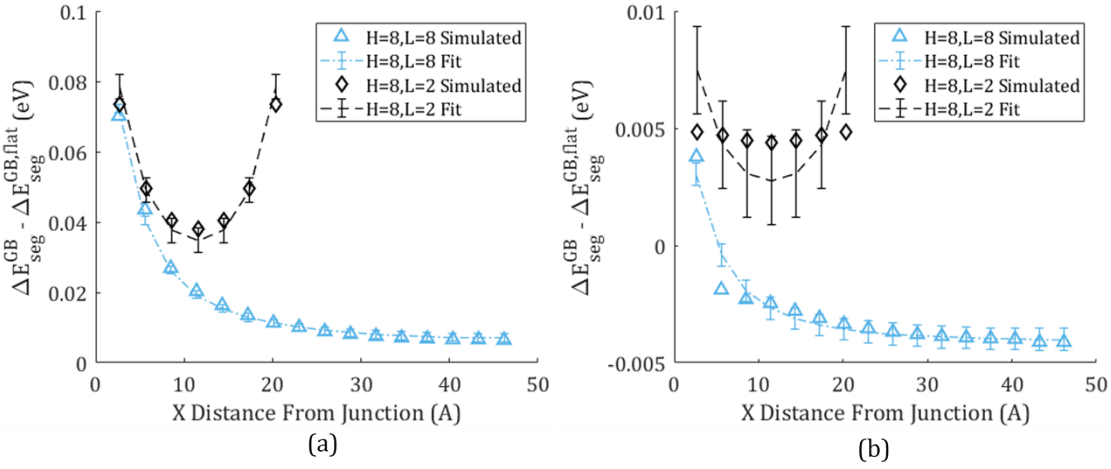

Figure 11: Model prediction overlayed with simulated segregation energy difference and RSE error bars for (a) Cu solutes with $c = 0.1009\ eV$, and (b) Ag solutes with $c = 0.0109\ eV$ along the horizontal line of atoms studied in Fig. 8. Note the difference in scale between (a) and (b).

Hence, the formula used to fit the segregation energy difference is,

$$\Delta E_{seg} - \Delta E_{seg}^{flat} = c \sum_{j} \frac{|\boldsymbol{b}_j \times \boldsymbol{r}_j|}{|\boldsymbol{r}_j|^2} + e\,. \tag{7}$$

Figure 11 shows the fit for two models, $H = 8, L = 8$ and $H = 8, L = 2$, along the same row of atoms studied in Fig. 8 Here, for a Cu solute in the GB model $c = 0.1009\ eV$, while $e = -0.00046\ eV$ for $H = 8, L = 8$ and $e = -0.00063\ eV$ for $H = 8, L = 2$. Meanwhile, for a Ag

solute in the GB model $c = 0.0109\ eV$, while $e = -0.00482\ eV$ for $H = 8, L = 8$ and $e = -0.00108\ eV$ for $H = 8, L = 2$. Error bars are provided using the RSE, and the plot considers the same row of atoms as in Fig. 8. For Cu, e is three orders of magnitude smaller than c, indicating the dominance of elastic hydrostatic stress effects in the segregation energy difference. Conversely for Ag, both e and c are both very small, on the order of $10^{-2} - 10^{-3}\ eV$, suggesting that both hydrostatic stresses, junction-junction and junction core effects are of similar importance for this solute.

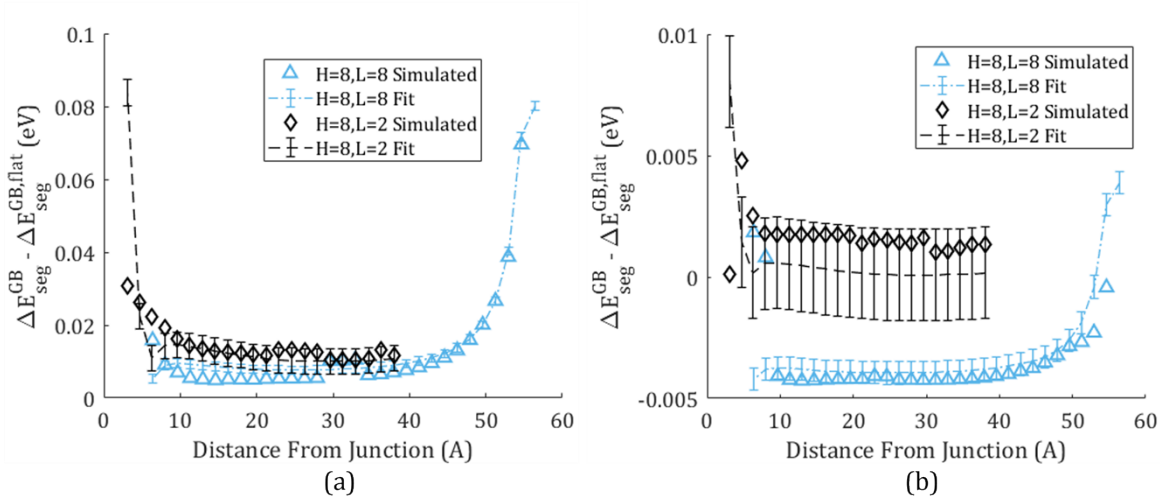

Figure 12: Model prediction overlayed with simulated segregation energy difference and RSE error bars on the sloped facet for (a) Cu solutes with $c = 0.1009\ eV$, and (b) Ag solutes with $c = 0.0109\ eV$ along the sloped line of atoms studied in Fig. 9. Note the difference in scale between (a) and (b).

Additionally, we take the above fit produced for the horizontal facet and apply it to the data along the sloped facet to determine how well the model extends to other regions of the faceted GB. Figure 12 shows the segregation energy difference along the sloped facet for Cu and Ag solutes, overlayed with the model. Although there is some noticeable deviation near the junctions, the model mostly captures the segregation energy difference data within

the model error. We conclude then that the summation of individual junction effects plus an additional term to account for higher-order effects as in Eq. (7) is an appropriate approximation of the segregation energy difference, and therefore a good model of the effect of junctions on segregation.

4.3. Relationship Between Junctions and Embrittlement

As shown in Fig. 8, contours of the embrittling potency difference and segregation energy difference as a function of separation distance have similar forms. Since embrittling potency is a difference of segregation energies, we can represent embrittlement with an analytical form similar to Eq. (5),

$$\Delta E_{b,i} = \Delta E_{b,i}^{flat} + E_{jxn} + E_{jxn-jxn} + E_{FS-jxn}\,. \tag{8}$$

Here, E_{FS-jxn} is an energy of interaction between the FS and the junctions. Again, E_{FS-jxn} is not an excess energy associated with the existence of FS-junction interaction, normalized by the line length of the junction, but specifically the change in segregation energy of a

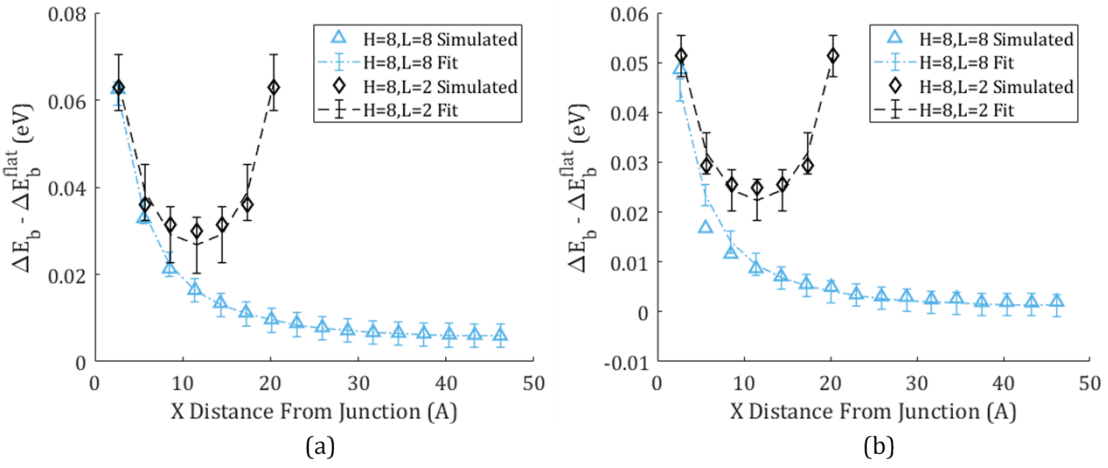

Figure 13: Model prediction and simulated embrittling potency difference and RSE error bars for (a) Cu solutes with $c = 0.0481\ eV$ and (b) Ag solutes with $c = 0.0151\ eV$ along the horizontal line of atoms studied in Fig. 8. Note the difference in scale between (a) and (b).

particular atomic site resulting from the interaction with the FS-junction feature. During fitting, E_{FS-jxn} is absorbed into the e term.

To obtain fits for the embrittling potency difference data, we first fit to the FS segregation energy difference data. For this FS fit, Cu has $c = 0.0528\ eV$ and Ag has $c = -0.0042\ eV$. The difference between GB and FS fit values provides the E_{jxn} constant for $\Delta E_{b,i} - \Delta E_{b,i}^{flat}$ data, due to Eq. (2). Hence, for the embrittling potency difference, the Cu constants are $c = 0.0481\ eV$, $e = -0.0040\ eV$ for $H = 8, L = 8$ and $e = -0.0099\ eV$ for $H = 8, L = 2$ and the Ag constants are $c = 0.0151\ eV$ and $e = -0.0036\ eV$ for $H = 8, L = 8$ and $e = -0.0025\ eV$ for $H = 8, L = 2$. The model is shown in Fig. 13 overlayed on the embrittling potency difference data for both Cu and Ag solutes, with corresponding error bars derived from the RSE. Additionally, model performance along the sloped facet is shown in Fig. 14. The values of e for both solutes lie in the $10^{-3}\ eV$ range, except for the $H = 8, L = 2$ case for Cu solutes, where junction interaction is notable higher. Meanwhile, the values of c lie in the $10^{-2}\ eV$ range consistently. Furthermore, even though Cu and Ag have opposite segregation

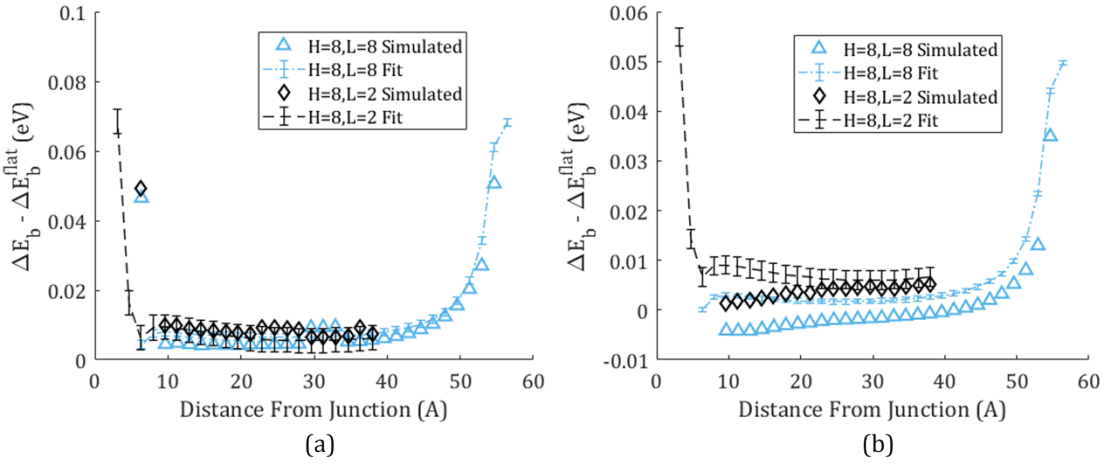

Figure 14: Model prediction and simulated embrittling potency difference and RSE error bars for (a) Cu solutes with $c = 0.0481\ eV$ and (b) Ag solutes with $c = 0.0151\ eV$ along the sloped line of atoms studied in Fig. 9. Note the difference in scale between (a) and

responses to hydrostatic stress, the presence of junctions increases the embrittling potency for both solute species. The choice of FS does not change this result either, as shown in the supplemental data in Figs. S4—S8. Hence, the elastic effects caused by proximity to the junction have a dominant effect on embrittlement.

Although error along the sloped facet is more substantial, the model still predicts a shift towards embrittlement near the junctions as suggested by the data. Nonetheless, the presence of the junction increases embrittling potency and proximity to the junction is the key factor in describing the magnitude of the enhanced embrittlement. Hence, junctions act as embrittling agents in a thermodynamic context for the chosen FS and atomic site type. These results may differ for anti-segregation sites.

It should be noted that different pro-segregation sites may show more embrittling, more strengthening, or even uninfluenced character in the presence of the junction. For a collective effect of the junction on solute embrittlement, it is pertinent to average the effect of junctions on different site types together, weighing the contribution of the effect to the average by the probability of occupancy of the respective atomic site [30,31]. Sites with more negative segregation energy are more likely to be occupied by solutes, and hence will more greatly contribute to the effect of junctions on embrittlement.

5. Conclusions

In this work, we investigate the impact of GB facet junctions on solute segregation and embrittlement. We compute data via atomistic simulations, using Cu and Ag solutes segregated to faceted Au $\Sigma 3$ $\langle 111 \rangle$ $\{112\}$ STGB models with varying distances between facet junctions. Additionally, for these models, we identify plausible FSs that result from fracture

by measuring excess surface energies. Through our study of 20 GB and FS models, we elucidate the effects of junctions on both segregation and embrittlement, through the geometry of the junction positions and hydrostatic stresses associated with the dislocation content. We emphasize that, despite the small excess effect of the junctions on segregation and embrittlement, the junction presence dominates solute distribution along the GB and strongly impact fracture resilience. Furthermore, we develop a simple model which estimates the energetic impact of junctions on segregation and embrittlement using the analytical stress fields of edge dislocations. The fitting parameter on the hydrostatic stress term is determined using the $H = 8, L = 8$ model while the fitting parameter accounting for higher-order effects, such as junction-junction interactions, is different for each model. Model validity is verified by comparing predictions with atomistic simulation data for all facet geometries. Effects represented by the fitting constant e are generally an order of magnitude less than the effect of hydrostatic stress fields combined with the fitting constant c; hence, the superposable effect of junction hydrostatic stress fields on embrittlement plays the most important role. We note that this first-order model is predicated on the existence of a dislocation at the core of the junction. We show that even though Cu and Ag have opposing segregation preferences, for the conditions studied, junctions consistently act as embrittling agents, such that the presence of the junction shifts the energetic landscape for all surrounding atoms, regardless of solute type, towards embrittlement.

Acknowledgements

M.F. and D.E.S. acknowledge support provided by Sandia National Laboratories and the University of Florida. R.D. and D.M. are supported by the U.S. Department of Energy

(DOE) Office of Basic Energy Sciences, Division of Materials Science and Engineering. The authors acknowledge University of Florida Research Computing for providing computational resources and support that have contributed to the research results reported in this publication. The work in this paper was performed, in part, at the Center for Integrated Nanotechnologies, an Office of Science User Facility operated for the U.S. DOE.

This article has been authored by an employee of National Technology & Engineering Solutions of Sandia, LLC under Contract No. DE-NA0003525 with the U.S. Department of Energy (DOE). The employee owns all rights, title, and interest in and to the article and is solely responsible for its contents. The United States Government retains and the publisher, by accepting the article for publication, acknowledges that the United States Government retains a non-exclusive, paid-up, irrevocable, world-wide license to publish or reproduce the published form of this article or allow others to do so, for United States Government purposes. The DOE will provide public access to these results of federally sponsored research in accordance with the DOE Public Access Plan https://www.energy.gov/downloads/doe-public-access-plan.

References

[1] V.M. Samoilov, B.G. Ostronov, Effect of Grain Size on the Modulus of Elasticity and Strength of Synthetic Graphites, Inorg. Mater. 40 (2004) 359–363. https://doi.org/10.1023/B:INMA.0000023955.17000.27.

[2] I. Simonovski, L. Cizelj, The Influence of the Grain Structure Size on Microstructurally Short Cracks, J. Eng. Gas Turbines Power 131 (2009). https://doi.org/10.1115/1.3079610.

[3] Q.P. Sun, Y.J. He, A multiscale continuum model of the grain-size dependence of the stress hysteresis in shape memory alloy polycrystals, Int. J. Solids Struct. 45 (2008) 3868–3896. https://doi.org/10.1016/j.ijsolstr.2007.12.008.

[4] V. Turlo, T.J. Rupert, Grain boundary complexions and the strength of nanocrystalline metals: Dislocation emission and propagation, Acta Mater. 151 (2018) 100–111. https://doi.org/10.1016/j.actamat.2018.03.055.
[5] H. Feng, J. Pang, Q. Fang, C. Chen, P. Wen, Enhanced ductility of nanomaterials through cooperative dislocation emission from cracks and grain boundaries, Int. J. Mech. Sci. 179 (2020) 105652. https://doi.org/10.1016/j.ijmecsci.2020.105652.
[6] P.R. Cantwell, M. Tang, S.J. Dillon, J. Luo, G.S. Rohrer, M.P. Harmer, Grain boundary complexions, Acta Mater. 62 (2014) 1–48. https://doi.org/10.1016/j.actamat.2013.07.037.
[7] S.J. Dillon, M. Tang, W.C. Carter, M.P. Harmer, Complexion: A new concept for kinetic engineering in materials science, Acta Mater. 55 (2007) 6208–6218. https://doi.org/10.1016/j.actamat.2007.07.029.
[8] S.J. Dillon, M.P. Harmer, Multiple grain boundary transitions in ceramics: A case study of alumina, Acta Mater. 55 (2007) 5247–5254. https://doi.org/10.1016/J.ACTAMAT.2007.04.051.
[9] M.P. Seah, Segregation and the strength of grain boundaries, 1976.
[10] D. Bouchet, L. Priester, Grain boundary plane and intergranular segregation in nickel-sulfur system, Scr. Metall. 21 (1987) 475–478. https://doi.org/10.1016/0036-9748(87)90184-0.
[11] X.-Y. Liu, J.B. Adams, Grain-boundary segregation in Al–10%Mg alloys at hot working temperatures, Acta Mater. 46 (1998) 3467–3476. https://doi.org/10.1016/S1359-6454(98)00038-X.
[12] S. Kobayashi, T. Maruyama, S. Tsurekawa, T. Watanabe, Grain boundary engineering based on fractal analysis for control of segregation-induced intergranular brittle fracture in polycrystalline nickel, Acta Mater. 60 (2012) 6200–6212. https://doi.org/10.1016/J.ACTAMAT.2012.07.065.
[13] T. Frolov, S.V. Divinski, M. Asta, Y. Mishin, Effect of interface phase transformations on diffusion and segregation in high-angle grain boundaries, Phys. Rev. Lett. 110 (2013). https://doi.org/10.1103/PhysRevLett.110.255502.
[14] P. Lejček, Effect of solute interaction on interfacial segregation and grain boundary embrittlement in binary alloys, J. Mater. Sci. 48 (2013) 2574–2580. https://doi.org/10.1007/s10853-012-7048-0.
[15] L. Zhao, R. He, A. Zabet-Khosousi, K.S. Kim, T. Schiros, M. Roth, P. Kim, G.W. Flynn, A. Pinczuk, A.N. Pasupathy, Dopant Segregation in Polycrystalline Monolayer Graphene, Nano Lett. 15 (2015) 1428–1436. https://doi.org/10.1021/nl504875x.
[16] D.E. Spearot, G.J. Tucker, A. Gupta, G.B. Thompson, Mechanical properties of stabilized nanocrystalline FCC metals, J. Appl. Phys. 126 (2019) 110901. https://doi.org/10.1063/1.5114706.
[17] J.M. Monti, E.M. Hopkins, K. Hattar, F. Abdeljawad, B.L. Boyce, R. Dingreville, Stability of immiscible nanocrystalline alloys in compositional and thermal fields, Acta Mater. 226 (2022) 117620. https://doi.org/10.1016/J.ACTAMAT.2022.117620.
[18] D.L. Medlin, K. Hattar, J.A. Zimmerman, F. Abdeljawad, S.M. Foiles, Defect character at grain boundary facet junctions: Analysis of an asymmetric Σ = 5 grain boundary in Fe, Acta Mater. 124 (2017) 383–396. https://doi.org/10.1016/j.actamat.2016.11.017.
[19] I. Daruka, J.C. Hamilton, Atomistic and Lattice Model of a Grain Boundary Defaceting Phase Transition, Phys. Rev. Lett. 92 (2004) 246105. https://doi.org/10.1103/PhysRevLett.92.246105.
[20] F. Abdeljawad, D.L. Medlin, J.A. Zimmerman, K. Hattar, S.M. Foiles, A diffuse interface model of grain boundary faceting, J. Appl. Phys. 119 (2016) 235306. https://doi.org/10.1063/1.4954066.
[21] Z.X. Wu, Y.W. Zhang, D.J. Srolovitz, Grain boundary finite length faceting, Acta Mater. 57 (2009) 4278–4287. https://doi.org/10.1016/j.actamat.2009.05.026.
[22] T.E. Hsieh, R.W. Balluffi, Observations of roughening/de-faceting phase transitions in grain boundaries, Acta Metall. 37 (1989) 2133–2139. https://doi.org/10.1016/0001-6160(89)90138-7.
[23] A.P. Sutton, R.W. Balluffi, Interfaces in Crystalline Materials, Oxford University Press, Oxford, New York, 2007.

[24] J.-E. Brandenburg, L.A. Barrales-Mora, D.A. Molodov, G. Gottstein, Motion of a grain boundary facet in aluminum, Acta Mater. 61 (2013) 5518–5524. https://doi.org/10.1016/j.actamat.2013.05.043.
[25] M.J. McCarthy, T.J. Rupert, Alloying induces directionally-dependent mobility and alters migration mechanisms of faceted grain boundaries, Scr. Mater. 194 (2021) 113643. https://doi.org/10.1016/j.scriptamat.2020.113643.
[26] C. Hu, S. Berbenni, D.L. Medlin, R. Dingreville, Discontinuous segregation patterning across disconnections, Acta Mater. 246 (2023) 118724. https://doi.org/10.1016/j.actamat.2023.118724.
[27] C. Hu, D.L. Medlin, R. Dingreville, Disconnection-Mediated Transition in Segregation Structures at Twin Boundaries, J. Phys. Chem. Lett. 12 (2021) 6875–6882. https://doi.org/10.1021/acs.jpclett.1c02189.
[28] N. Tuchinda, C.A. Schuh, Triple junction solute segregation in Al-based polycrystals, Phys. Rev. Mater. 7 (2023) 023601. https://doi.org/10.1103/PhysRevMaterials.7.023601.
[29] J.R. Rice, J.-S. Wang, Embrittlement of interfaces by solute segregation, Mater. Sci. Eng. A 107 (1989) 23–40. https://doi.org/10.1016/0921-5093(89)90372-9.
[30] D. Aksoy, R. Dingreville, D.E. Spearot, Spectrum of embrittling potencies and relation to properties of symmetric-tilt grain boundaries, Acta Mater. 205 (2021) 116527. https://doi.org/10.1016/j.actamat.2020.116527.
[31] M.E. Fernandez, R. Dingreville, D.E. Spearot, Statistical perspective on embrittling potency for intergranular fracture, Phys. Rev. Mater. 6 (2022) 083602. https://doi.org/10.1103/PhysRevMaterials.6.083602.
[32] P.K. Kristensen, C.F. Niordson, E. Martínez-Pañeda, Applications of phase field fracture in modelling hydrogen assisted failures, Theor. Appl. Fract. Mech. 110 (2020) 102837. https://doi.org/10.1016/j.tafmec.2020.102837.
[33] E. Martínez-Pañeda, A. Golahmar, C.F. Niordson, A phase field formulation for hydrogen assisted cracking, Comput. Methods Appl. Mech. Eng. 342 (2018) 742–761. https://doi.org/10.1016/j.cma.2018.07.021.
[34] S. Serebrinsky, E.A. Carter, M. Ortiz, A quantum-mechanically informed continuum model of hydrogen embrittlement, J. Mech. Phys. Solids 52 (2004) 2403–2430. https://doi.org/10.1016/j.jmps.2004.02.010.
[35] R.C. Pond, D.L. Medlin, A. Serra, A study of the accommodation of coherency strain by interfacial defects at a grain boundary in gold, Philos. Mag. 86 (2006) 4667–4684. https://doi.org/10.1080/14786430600698864.
[36] F. Ernst, M.W. Finnis, D. Hofmann, T. Muschik, U. Schönberger, U. Wolf, M. Methfessel, Theoretical prediction and direct observation of the 9 *R* structure in Ag, Phys. Rev. Lett. 69 (1992) 620–623. https://doi.org/10.1103/PhysRevLett.69.620.
[37] U. Wolf, F. Ernst, T. Muschik, M.W. Finnis, H.F. Fischmeister, The influence of grain boundary inclination on the structure and energy of σ = 3 grain boundaries in copper, Philos. Mag. A 66 (1992) 991–1016. https://doi.org/10.1080/01418619208248003.
[38] C.B. Carter, D.L. Medlin, J.E. Angelo, M.J. Mills, The 112 Lateral Twin Boundary in FCC Materials, Mater. Sci. Forum 207–209 (1996) 209–212. https://doi.org/10.4028/www.scientific.net/MSF.207-209.209.
[39] D.L. Medlin, G.H. Campbell, C.B. Carter, Stacking defects in the 9R phase at an incoherent twin boundary in copper, Acta Mater. 46 (1998) 5135–5142. https://doi.org/10.1016/S1359-6454(98)00164-5.
[40] T. Tsuru, H. Somekawa, D.C. Chrzan, Interfacial segregation and fracture in Mg-based binary alloys: Experimental and first-principles perspective, Acta Mater. 151 (2018) 78–86. https://doi.org/10.1016/j.actamat.2018.03.061.

[41] A. Kumar, J. Wang, C.N. Tomé, First-principles study of energy and atomic solubility of twinning-associated boundaries in hexagonal metals, Acta Mater. 85 (2015) 144–154. https://doi.org/10.1016/j.actamat.2014.11.015.
[42] J.F. Nie, Y.M. Zhu, J.Z. Liu, X.Y. Fang, Periodic Segregation of Solute Atoms in Fully Coherent Twin Boundaries, Science 340 (2013) 957–960. https://doi.org/10.1126/science.1229369.
[43] A.P. Thompson, H.M. Aktulga, R. Berger, D.S. Bolintineanu, W.M. Brown, P.S. Crozier, P.J. in 't Veld, A. Kohlmeyer, S.G. Moore, T.D. Nguyen, R. Shan, M.J. Stevens, J. Tranchida, C. Trott, S.J. Plimpton, LAMMPS - a flexible simulation tool for particle-based materials modeling at the atomic, meso, and continuum scales, Comput. Phys. Commun. 271 (2022) 108171. https://doi.org/10.1016/j.cpc.2021.108171.
[44] A. Stukowski, Visualization and analysis of atomistic simulation data with OVITO–the Open Visualization Tool, Model. Simul. Mater. Sci. Eng. 18 (2010) 015012. https://doi.org/10.1088/0965-0393/18/1/015012.
[45] X.W. Zhou, R.A. Johnson, H.N.G. Wadley, Misfit-energy-increasing dislocations in vapor-deposited CoFe/NiFe multilayers, Phys. Rev. B 69 (2004) 144113. https://doi.org/10.1103/PhysRevB.69.144113.
[46] C. Hu, Y. Li, Z. Yu, J. Luo, Computing grain boundary diagrams of thermodynamic and mechanical properties, Npj Comput. Mater. 7 (2021) 159. https://doi.org/10.1038/s41524-021-00625-2.
[47] C.T. Forwood, M.A. Gibson, Rigid-body displacements at incoherent 112 Σ = 3 boundaries in Ni3Al, Philos. Mag. Lett. 65 (1992) 331–337. https://doi.org/10.1080/09500839208206004.
[48] R.C. Pond, D.A. Smith, W. a. T. Clark, An experimental study of coincidence grain boundary structure using displacement fringes, J. Microsc. 102 (1974) 309–316. https://doi.org/10.1111/j.1365-2818.1974.tb04642.x.
[49] J.W. Matthews, W.M. Stobbs, Measurement of the lattice displacement across a coincidence grain boundary, Philos. Mag. J. Theor. Exp. Appl. Phys. 36 (1977) 373–383. https://doi.org/10.1080/14786437708244941.
[50] J.P. Hirth, J. Lothe, Theory of Dislocations, Wiley, 1982.
[51] C.J. McMahon, Hydrogen-induced intergranular fracture of steels, Eng. Fract. Mech. 68 (2001) 773–788. https://doi.org/10.1016/S0013-7944(00)00124-7.
[52] H.L. Mai, X.-Y. Cui, D. Scheiber, L. Romaner, S.P. Ringer, Phosphorus and transition metal co-segregation in ferritic iron grain boundaries and its effects on cohesion, Acta Mater. 250 (2023) 118850. https://doi.org/10.1016/j.actamat.2023.118850.
[53] H.L. Mai, X.-Y. Cui, D. Scheiber, L. Romaner, S.P. Ringer, An understanding of hydrogen embrittlement in nickel grain boundaries from first principles, Mater. Des. 212 (2021) 110283. https://doi.org/10.1016/j.matdes.2021.110283.
[54] H.L. Mai, X.-Y. Cui, D. Scheiber, L. Romaner, S.P. Ringer, The segregation of transition metals to iron grain boundaries and their effects on cohesion, Acta Mater. 231 (2022) 117902. https://doi.org/10.1016/j.actamat.2022.117902.
[55] D. McLean, Grain boundaries in metals, Clarendon Press, 1957.
[56] C.L. White, W.A. Coghlan, The spectrum of binding energies approach to grain boundary segregation, Metall. Trans. A 8 (1977) 1403–1412. https://doi.org/10.1007/BF02642853.
[57] C.L. White, D.F. Stein, Sulfur segregation to grain boundaries in Ni3Al and Ni3(Al,Ti) alloys, Metall. Trans. A 9 (1978) 13–22. https://doi.org/10.1007/BF02647165.
[58] C.L. Kelchner, S.J. Plimpton, J.C. Hamilton, Dislocation nucleation and defect structure during surface indentation, Phys. Rev. B 58 (1998) 11085–11088. https://doi.org/10.1103/PhysRevB.58.11085.
[59] C.A. Schuh, K. Lu, Stability of nanocrystalline metals: The role of grain-boundary chemistry and structure, MRS Bull. 46 (2021) 225–235. https://doi.org/10.1557/s43577-021-00055-x.

[60] Z.A.D. Lethbridge, R.I. Walton, A.S.H. Marmier, C.W. Smith, K.E. Evans, Elastic anisotropy and extreme Poisson's ratios in single crystals, Acta Mater. 58 (2010) 6444–6451. https://doi.org/10.1016/j.actamat.2010.08.006.
[61] G.P. Dimitrakopulos, Ph. Komninou, Th. Karakostas, R.C. Pond, Junction Line Disclinations: Characterisation and Observations, Interface Sci. 7 (1999) 217–229. https://doi.org/10.1023/A:1008713124286.
[62] A.A. Nazarov, O.A. Shenderova, D.W. Brenner, On the disclination-structural unit model of grain boundaries, Mater. Sci. Eng. A 281 (2000) 148–155. https://doi.org/10.1016/S0921-5093(99)00727-3.
[63] R. Dingreville, S. Berbenni, On the interaction of solutes with grain boundaries, Acta Mater. 104 (2016) 237–249. https://doi.org/10.1016/j.actamat.2015.11.017.